NANO LETTERS

LETTER

pubs.acs.org/NanoLett

Nanoepitaxy Using Micellar Nanoparticles

F. Behafarid and B. Roldan Cuenya*

Department of Physics, University of Central Florida, Orlando, Florida 32816, United States

Supporting Information

ABSTRACT: The shape of platinum and gold nanoparticles (NPs) synthesized via inverse micelle encapsulation and supported on TiO_2(110) has been resolved by scanning tunneling microscopy. Annealing these systems at high temperature (~1000 °C) and subsequent cooling to room temperature produced ordered arrays of well-separated three-dimensional faceted NPs in their equilibrium state. The observed shapes differ from the kinetically limited shapes of conventional physical vapor deposited NPs, which normally form two-dimensional flat islands upon annealing at elevated temperatures. The initial NP volume was found to provide a means to control the final NP shape. Despite the liquid-phase ex situ synthesis of the micellar particles, the in situ removal of the encapsulating ligands and subsequent annealing consistently lead to the development of a well-defined epitaxial relationship of the metal NPs with the oxide support. The observed epitaxial relationships could be explained in terms of the best overlap between the interfacial Pt (or Au) and TiO_2 lattices. In most cases, the ratio of {100}/{111} facets obtained for the NP shapes resolved clearly deviates from that of conventional bulklike Wulff structures.

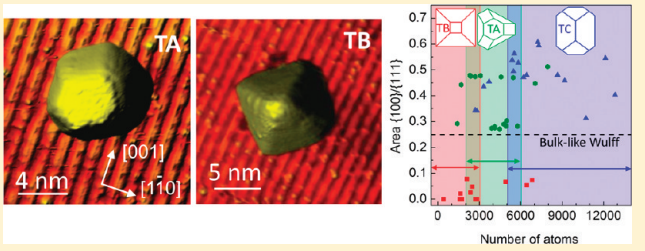

KEYWORDS: Nanoparticle, shape, STM, epitaxy, Pt, Au

Metal nanoparticles are currently being used in a variety of applications in the fields of plasmonics, magnetism, and catalysis.[1−3] Since many of the unusual electronic, optical, magnetic, and chemical properties of NPs have been shown to be size-, shape-, and strain-dependent,[3−10] control of these parameters could be used to optimize NP performance in a range of applications.[9,11] For example, a good epitaxial relationship would lead to significant improvements in the photocatalytic performance of the Pt/TiO_2 system through the facilitation of electron transfer processes from the substrate to the NPs.[9] Additionally, for small NPs, an epitaxial relationship with the substrate could lead to a degree of lattice strain that could otherwise not be obtained, which in turn may affect catalytic activity.[9,10] Finally, different epitaxial relationships could also affect the faceting of the NPs and thus potentially enhance the performance of the nanocatalysts. Therefore, determining and ultimately being able to tune such orientations could lead to major breakthroughs in this field. However, the preparation of high densities of 3D epitaxial NPs presents a challenge for most materials systems grown via physical vapor deposition (PVD), sputtering, and other synthesis methods, with most systems producing highly anisotropic or island-like structures.

In addition to fabrication challenges, the investigation of epitaxial NPs presents significant characterization challenges. Several attempts have been made to solve the structure of supported metallic NPs via ensemble-averaging methods.[12−14] For example, by use of angle-resolved X-ray photoelectron spectroscopy (XPS),[12] low-energy electron diffraction (LEED),[12,15] and X-ray photoelectron diffraction (XPD) techniques,[16] the dominant orientation of PVD-deposited Pt NPs on TiO_2(110) was found to be {111}. However in order to evaluate different NP/support epitaxial orientations which might coexist within the same sample, spatially resolved nonaveraging techniques such as transmission electron microscopy (TEM) or scanning tunneling microscopy (STM) are required. STM can routinely provide atomically resolved images on flat surfaces[17] and large 2D NPs with flat top facets.[18−21] However, when three-dimensional nanosized features are present on a surface, a larger fraction of the tip apex is involved in the imaging process, and tip convolution effects smear out the geometrical features of the NPs. In the present work, the use of ultrasharp tips enables partial imaging of select side facets of small (2−6 nm) 3D NPs, allowing the determination of their shape.

Our study illustrates how an ex situ chemical synthesis method, namely, inverse micelle encapsulation, can be used to achieve well-defined and tunable 3D NP shapes with epitaxial NP/support interfaces and how the size of the micellar NPs can be used to control their final shape and their epitaxial orientation on the support. Furthermore, we demonstrate that this method can produce NP shapes that significantly deviate from the common bulklike Wulff structures.

Experimental Section. Self-assembled size-selected Pt NPs were synthesized by micelle encapsulation.[22] Polystyrene-*block*-poly(2-vinylpyridine) [PS(x)-P2VP(y)] with different molecular weights were dissolved in toluene to form reverse micelles. To prepare NPs with a variety of sizes, different polymers with atomic weights (x:y) of (27700:4300), (81000:14200), and

Received: August 8, 2011
Revised: October 6, 2011
Published: October 25, 2011

dx.doi.org/10.1021/nl2027525 | *Nano Lett.* 2011, 11, 5290–5296

(81000:21000) were used. Subsequently, H_2PtCl_6 or $HAuCl_4$ was added at a metal salt/P2VP concentration ratio ranging from 0.01 to 0.6. The NP size is controlled by the length of the polymer head (P2VP) and the metal-salt/P2VP concentration ratio, while the interparticle distance is determined by the length of the polymer tail (PS).[22,23] Planar samples were prepared using a dip-coating method resulting in a monolayer-thick film of self-assembled micellar NPs on the substrate. Two Pt and one Au samples were investigated. Prior to the NP deposition, single crystal $TiO_2(110)$ substrates were cleaned in ultrahigh vacuum (UHV) by cycles of Ar^+ sputtering (1 keV) at room temperature (RT) and annealing at 1000 °C. The encapsulating polymer was removed in situ by an O_2-plasma treatment (4×10^{-5} mbar, 120 min). X-ray photoelectron spectroscopy measurements of the C-1s core level region corroborated the complete removal of the organic ligands.[24] Subsequently, the samples were isochronally annealed in UHV in 100 °C intervals for 20 min from 300 to 900 °C and for 10 min from 1000 to 1060 °C. This treatment resulted in the reduction of the PtO_x species formed upon O_2-plasma exposure. By variation of the molecular weight of the encapsulating polymer, metal salt loading, and thermal treatment (temperature and time), a variety of final NP volumes could be obtained, while keeping individual NPs well separated from each other on the TiO_2 surface. Figure 2 describes schematically the NP synthesis process: (a) micelle-encapsulated spherical NPs with no contact with the support; (b) ligand-free long-range-ordered single grain NPs resulting from the exposure to an O_2-plasma in UHV. An increase in the roughness of the support after this treatment is evidenced. At this stage, the NPs make contact with the support but their shape remains spherical;[25,26] (c) reduction and flattening of the TiO_2 support after high temperature annealing (1000 °C) accompanied by enhanced mobility of metal atoms within the NPs allowing them to rearrange and obtain a good interface matching; (d) well-faceted NPs with an epitaxial relation with the support obtained upon cooling to RT.

All STM images were acquired at RT (Aarhus-SPECS) after sample annealing at temperatures above 1000 °C. The chemically etched tungsten tips used were cleaned in situ via Ar^+ sputtering.

Results and Discussion. Figure 1 displays STM images that demonstrate the four main NP shape categories that were observed on $TiO_2(110)$ after the micellar NP formation and subsequent high temperature annealing.

All NPs show pronounced faceting and a clear orientation relative to the substrate's crystalline directions. On the basis of the observed relative angles of the various facets, the orientation of the free and interfacial Pt surfaces could be identified, as shown in Figure 1e–h. Type A (TA), type B (TB), and type D (TD) NPs have flat top facets while type C (TC) has a wedge. The interfacial facets of each NP category are: {111} for TA, {100} for TB, and {110} for TC and TD. Although TA and TD NPs have in common a hexagonal top facet, the angles between the edges on the top facet are ~125° and ~110° for TD NPs, in contrast with 120° for TA NPs. In addition, TD NPs have 2-fold rotational symmetry, while TA NPs have 3-fold symmetry. NP shapes of TA and TB, although with a much smaller height/diameter aspect ratio, were also observed for large NPs synthesized via PVD following a seeding growth method along the crystalline orientation of the seed.[19,20] However, to the best of our knowledge, TC and TD NPs have not been previously reported. Large Pt NPs (~30–100 nm) of TC shape were

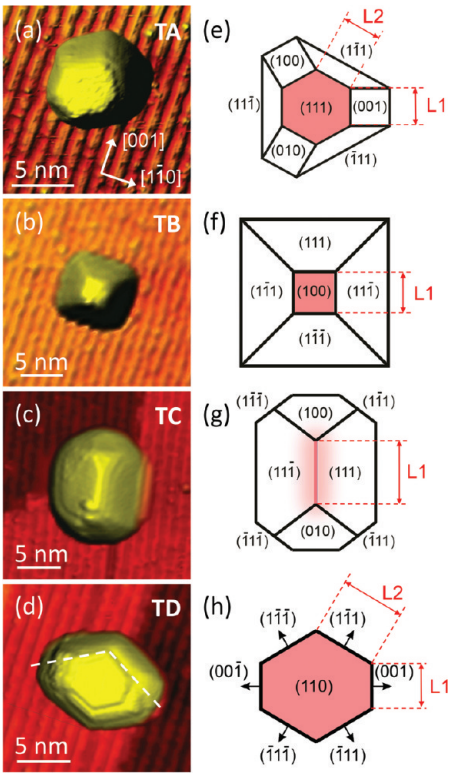

Figure 1. STM images of micellar Pt NPs supported on $TiO_2(110)$ acquired at RT after annealing at 1000 °C. The four main categories of NP shapes are displayed (a–d) together with the corresponding models (e–h). The facets at the perimeter of TD NPs are perpendicular to the NP/support interface and the apparent slopes observed around them in (d) are due to tip convolution effects.

however fabricated via electron beam lithography on $SrTiO_3$-(110) substrates.[6]

The observations made in Figure 1 can be understood by the structural evolution of the NPs schematically depicted in Figure 2a–d. Since the largely metallic core of the micelles is originally surrounded by polystyrene (PS) groups, there is no contact between the NP core and the oxide support after deposition. Therefore, no preferential decoration sites on the support surface are initially available for the micellar NPs. This is evidenced by the persistence of the hexagonal NP arrangement obtained after dip-coating, with an interparticle spacing determined by the length of the encapsulating PS groups,[27] Figure 2e,f. The atomic force microscopy (AFM) images shown in Figure 2g, h, which were acquired on similarly prepared Pt NPs, illustrate that different interparticle distances can be achieved via the micellar synthesis method when two diblock-copolymers with different tail length (PS group) are used. This is in clear contrast with the observations made for PVD metal NPs on TiO_2, which are known to preferentially nucleate at defect sites such as step edges or vacancy sites.[28,29] After the removal of the polymer (O_2-plasma in UHV), the NPs come in contact with the TiO_2-(110) substrate. Subsequent annealing above 1000 °C leads to surface and/or bulk melting of the NPs, and the minimization of their surface energy results in thermodynamically stable shapes. Our STM study, carried out at RT after the former treatment, demonstrates the stabilization of isolated faceted

dx.doi.org/10.1021/nl2027525 |Nano Lett. 2011, 11, 5290–5296

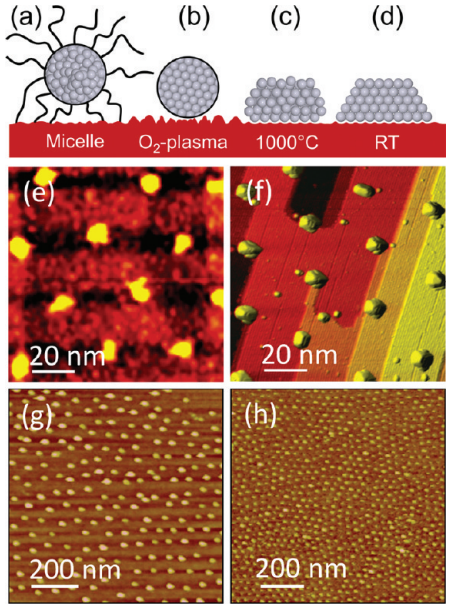

Figure 2. Schematic representation of the evolution of the structure of micellar NPs supported on TiO_2 after different chemical and thermal treatments (a–d). STM images of polymer-free micellar Pt NPs on TiO_2(110) acquired at RT after annealing at (e) 150 and (f) 1000 °C are also shown. The hexagonal NP arrangement is observed in (e) but also significant roughness of the TiO_2 support. A flatter and atomically resolved TiO_2 surface with shape-resolved Pt NPs is evident in (f). Large scale AFM images of micellar Pt NPs prepared using two different PS(x)-P2VP(y) diblock copolymers with (x, 27700; y, 4300) in (g) and (x, 53000; y, 43800) in (h). The images were acquired at RT after polymer removal.

single grain Pt and Au NPs with an epitaxial relation with the TiO_2(110) support, Figures 1 and 2f.

The NPs shapes, facet configurations, and epitaxial relationship with the TiO_2 support shown here for micellar NPs are not limited to the Pt/TiO_2 system, which is known for its strong metal–support interaction (SMSI) effect.[30,31] To illustrate this, Figure 3 shows similar faceting and epitaxial orientation for identically prepared (micelle synthesis) Au NPs on TiO_2(110). Panels a and b of Figure 3 show Au NPs of TA and TB, similar to the shapes observed for the Pt NPs. However, Au NPs of type C show a different shape than those observed for Pt, namely, they were found to be ~19° tilted along the TiO_2(110)-[001] axis, as shown in Figure 3c. The direction in which these NPs were sidewise tilted was found to be random and independent from the scanning direction selected. The cross section profile of the latter STM image is shown in Figure 3d (bottom) together with the corresponding model of the NP configuration and facet in contact with the TiO_2 support, in this case {221}. Another high-index Miller lattice orientation, {211}, was previously observed for Au/TiO_2 using electron backscattered diffraction techniques,[14] but not for Pt/TiO_2.

Variations in the ratio of {100}/{111} facet areas (A_{100}/A_{111}) within each category of NP shapes were observed, and examples are shown in Figure 4. For instance, the {100} top square facet in TB NPs, Figure 1b is absent for some NPs, leading to truncated octahedron shapes, Figure 4d. Since the highest morphological points of each category of NPs (shaded areas in Figure 1e–h) are the least likely to be affected by artifacts related to tip convolution effects, they can be used to reconstruct the NP shape and to obtain the area of different

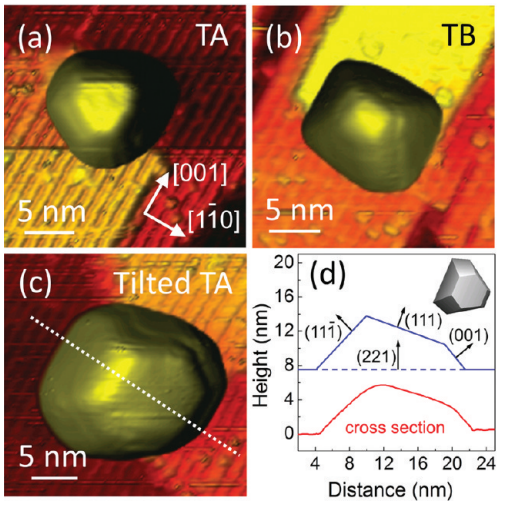

Figure 3. STM images of micellar Au NPs on TiO_2(110) acquired at RT after sample annealing at 1000 °C. The following NP shapes are shown: (a) TA, (b) TB, and (c) tilted TA. The STM cross section of the NP in (c) (along the dotted line) and a schematic of the corresponding facets are shown in (d). A Au(211) facet was found at the NP/support interface. The inset in (d) shows a model of the reconstructed NP shape.

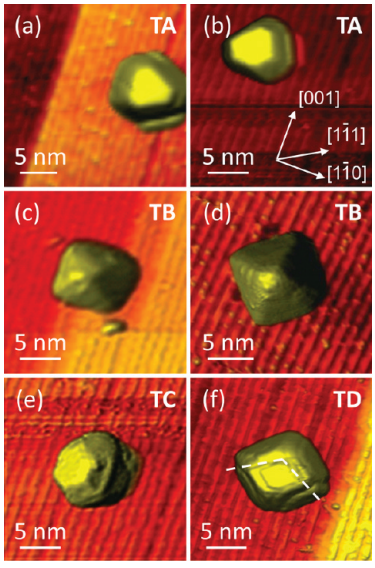

Figure 4. STM images of micellar Pt NPs on TiO_2(110) acquired at RT after annealing at 1000 °C. Examples of variations in the shapes of NPs within a given category (TA-TD) based on distinct A_{100}/A_{111} ratios are shown (panels a, c, e, and f). NPs of TA, TB, and TD in (panels a, c, and f) have a lower A_{100}/A_{111} ratio than those in panels a, b, and d of Figure 1, respectively. In rare cases, some NPs were found to be rotated by (b) 30° (TA) and (d) 45° (TB) with respect to the TiO_2(110)-[001] direction.

facets as well as the number of atoms in each NP. A more detailed description of this procedure is given in Supplementary Figure 1 in the Supporting Information. It should be however noted that despite the finite degree of shape heterogeneity reported in Figures 1, 3, and 4 including STM data acquired on three differently synthesized Au and Pt NP samples, a single initial narrow NP size distribution was found to lead to a relatively well-defined particle shape distribution.

dx.doi.org/10.1021/nl2027525 |*Nano Lett.* 2011, 11, 5290–5296

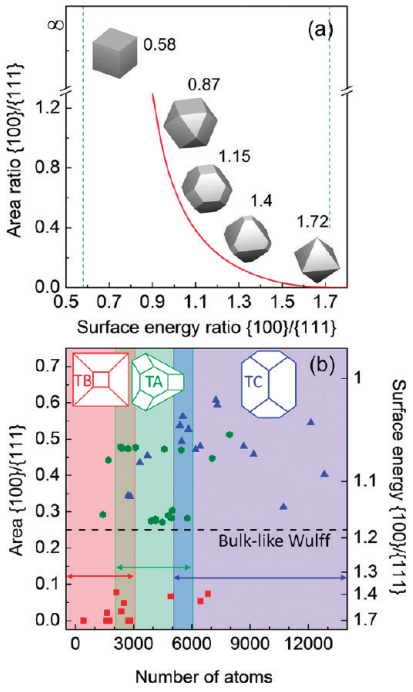

Figure 5. (a) Ratios of {100}/{111} surface areas (A_{100}/A_{111}) as a function of the corresponding surface energy ratios ($\gamma_{100}/\gamma_{111}$) following the Wulff theorem. Representative model NP shapes are shown as inset. For $\gamma_{100}/\gamma_{111} > 1.7$, no {100} facets are present, and the NPs adopt octahedron shapes. For $0.87 < \gamma_{100}/\gamma_{111} < 1.15$, the NPs adopt cuboctahedron and truncated cuboctahedron shapes. For $\gamma_{100}/\gamma_{111} < 0.58$, cubic shapes are found. (b) STM-resolved A_{100}/A_{111} ratios (left axis) and corresponding $\gamma_{100}/\gamma_{111}$ ratios (right axis) obtained from (a) plotted versus the number of atoms within each NP. Schematics of the NP shapes observed are included as insets in (b).

Following Wulff's theory,[32] a variety of equilibrium shapes can be obtained for unsupported NPs depending on the surface energy (γ) ratio of different facets (i.e., $\gamma_{100}/\gamma_{111}$), since distinct facets are characterized by different surface energies. An example of theoretical Wulff shapes is shown in Figure 5a, where the A_{100}/A_{111} ratio is plotted versus the respective $\gamma_{100}/\gamma_{111}$. Figure 5b (left axis) shows the experimental A_{100}/A_{111} ratio as a function of the number of atoms in each NP for the three categories of shapes most commonly observed via STM. The range of NP sizes (or number of atoms) giving rise to NPs of TA is highlighted by green shading, those of TB by red, and TC by a blue background. Since the majority of the experimental TiO_2-supported Pt NPs display shapes analogous to those theoretically predicted for the unsupported Wulff model NPs, but truncated in half, the experimental surface area ratios are expected to be similar to those of the Wulff structures. Accordingly, Figure 5a can be used to extract the $\gamma_{100}/\gamma_{111}$ ratio of the STM-resolved NPs, Figure 5b (right axis).

The A_{100}/A_{111} ratio is 0.25 for a truncated cuboctahedron NP (bulklike Wulff shape typical of large NPs).[33−35] However, different geometrical characteristics were observed here for the micellar Pt NPs, with $A_{100}/A_{111} < 0.25$ for TB NPs and >0.25 for TA and TC. The corresponding surface energy ratios are $\gamma_{100}/\gamma_{111} > 1.4$ for TB NPs, and $\gamma_{100}/\gamma_{111} < 1.2$ for TA and TC. Since these shapes were obtained for NPs preannealed above 1000 °C, they are considered to be the most thermodynamically stable shapes for this system. The observed deviations from bulklike Wulff structures ($\gamma_{100}/\gamma_{111} = 1.18$)[33,34,36] might be due to finite size effects, interface-induced stress, and adsorbate effects.[37,38] Interestingly, Figure 5b demonstrates that the majority of TB NPs (>75%) have less than 3000 atoms, while the majority of TA NPs (>75%) contain 2000−6000 atoms. Type C NPs are the largest among these three categories, with 75% of the NPs having more than 5000 atoms. A similar shape transition was predicted theoretically with increasing NP size for Pt NPs on MgO.[39] These data highlight that the dominant shape of the NPs formed via the present micellar synthesis method on a given substrate can be controlled by tuning their initial size distribution, provided that no sintering phenomena take place. The enhanced stability against coarsening and lack of mobility of our micellar NPs after severe thermal treatments was previously demonstrated.[27] The latter trend is assigned to the narrow initial NP size distributions and large interparticle spacings attained by this synthetic route and to the fact that no isolated atoms (highly mobile) are originally present in between NPs in these samples.

Interestingly, all of our NPs have an epitaxial relationship with the underlying substrate, since one of the NPs' symmetry axes is always parallel to the TiO_2(110) rows. As demonstrated in Figure 2e, such an epitaxial relation does not exist after NP deposition and moderate annealing (150 °C) and should have developed as a result of the high-temperature annealing (1000 °C). Although in most cases the NPs have two edges parallel to the TiO_2(110)-[100] rows (Figures 1 and 4a,c,e), a few examples of NPs rotated by 30° (Figure 4b) or 45° (Figure 4d) without any edge parallel to the TiO_2(110)-[100] direction can also be found. However, even for these rare cases, one of the symmetry axes of the NPs is parallel to the TiO_2(110)-[100] rows, demonstrating the existence of an epitaxial relation with the support. Such exceptions were not found for TC Pt NPs, with the top edge being always parallel to the TiO_2 rows. Type D Pt NPs were very rare and insufficient statistics could be obtained for this category.

A major difference between our micellar NPs and PVD NPs is the growth mechanism. While micellar NPs are deposited on the substrate preformed, the evaporated NPs grow on the surface via the adsorption of diffusing metal adatoms. Therefore, in the latter case, the anisotropy of the substrate surface plays a crucial role in determining the growth kinetics and final NP shape. For example, the lowest diffusion coefficient for Pt adatoms on stoichiometric TiO_2(110) has been found to be along the [001] direction.[40] The latter might be responsible for the more asymmetric NP shapes of PVD-prepared NPs, which appear elongated along [001][19,20] in contrast to symmetric shapes observed for our micellar NPs. Metal NPs have been shown to affect the surface segregation of oxygen vacancies in TiO_2 substrates.[41] The possible existence of different vacancy concentrations underneath the NPs in NP samples prepared by PVD versus our micellar method might result in different NP/support binding energies and, consequently, in different NP shapes.

Several procedures have been developed in the past in order to gain control over the shape of NPs based on altering the growth rate of different facet orientations.[5,42,43] Although good shape-selection results from some of these methods, the morphologies obtained are mainly dominated by growth kinetics, and such structures are not thermodynamically stable. Therefore, they cannot withstand the environmental conditions that some applications might require (e.g., high-temperature catalytic reactions).[44] The enhanced thermal stability displayed by our micellar NPs[27] has allowed us to resolve the shapes of small NPs after annealing at high temperature (>1000 °C), which is expected to result in the most

dx.doi.org/10.1021/nl2027525 |Nano Lett. 2011, 11, 5290–5296

thermodynamically favored NP geometries. Since in theoretical calculations the clusters are allowed to relax and to find the energy minima, the equilibrium shapes obtained for the micellar NPs are expected to be much better models for comparison with theoretical calculations of face-centered cubic clusters.[45]

As was mentioned in the introduction, not just their epitaxial relation but also the specific orientation of the NPs on the support is important for their application in catalysis and other fields.[9] For this reason, the lattice matching and interfacial strain were also obtained. In order to explain the epitaxial orientation of the annealed micellar NPs on $TiO_2(110)$, for a given interfacial Pt plane, the corresponding facets were superimposed to the TiO_2 surface lattice and rotated about an axis perpendicular to the interface. This procedure follows the "coincidence of reciprocal lattice points" method (CRLP),[46] but has been modified to describe real-space 2D lattices found at the NP/support interface. Following this approach, the number of Pt atoms overlapping with the TiO_2 lattice was calculated after allowing a certain expansion/compression (strain, ε) of the Pt lattice in the [001] (ε_x) and [1$\bar{1}$0] (ε_y) directions of $TiO_2(110)$. An example of the results of this procedure is given in Figure 6. Additional details on the calculation method and the relaxations of the Pt lattice obtained for several different Pt facet orientations can be found in the Supplementary Table 1 and Supplementary Figure 2 in the Supporting Information. The optimum rotation angles were found to be zero for all configurations, resulting in one edge of the NPs being parallel to the $TiO_2(110)$-[001] direction, as observed in our experiments.

Figure 6a shows the overlap between a strained Pt(111) overlayer and $TiO_2(110)$, representative of TA NPs, as a function of the in-plane rotation angle (θ) of the Pt(111) facet and strain coefficient ε_x for the optimum ε_y of 10%. As explained in more detail in the Supporting Information, ε is defined as $100 \times (L_{bulk} - L_{relaxed})/L_{bulk}$, where L is the dimension of the Pt surface lattice unit cell in the x or y direction. A positive (negative) value of ε represents the contraction (expansion) of the interfacial Pt lattice in contact with TiO_2. The optimum strain values, e.g., those leading to the maximum interfacial overlap of Pt (or Au) and TiO_2 lattices, are shown in Supplementary Tables 1 and 2 in the Supporting Information. An analogous analysis carried out for the rotated TA NP in Figure 4b is shown in Figure 6c,d. However, it should be noted that the maximum Pt/TiO_2 interfacial overlap obtained for this rotated NP is much smaller than that of the regular TA NP (Supplementary Table 1 in the Supporting Information). The latter explains their rare appearance. Although our calculations reveal strain values for the Pt and Au lattices of up to ~10%, due to the simplicity of the model used, these findings should not be overstressed, since they do not take into consideration the concomitant possible relaxation of the TiO_2 support underneath the NPs.[47]

Previous calculations by Muller et al.[48,49] predicted that interfacial strain could affect the area of specific facets in small NPs. Furthermore, in some cases, a slight change in the NP size was found to lead to discontinuities in the surface energy and unusual relative contributions of different facets. Such an effect might explain the shape variations observed within a given NP category for NPs with nearly identical volume (or total number of atoms), Figure 5. For small supported NPs, interfacial stress likely extends throughout the NP, resulting in a change of the energy of surface facets having a component parallel to the direction of the stress vector. Accordingly, top NP facets parallel to the interface should be the most affected by the former effect. Similar tensile

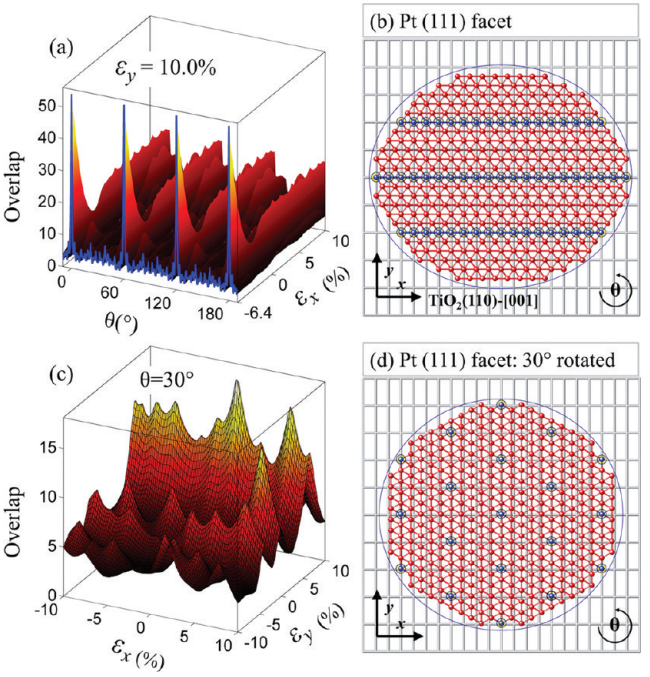

Figure 6. (a, c) Calculations of the epitaxial relationship between Pt(111) interfacial facets in TA NPs and the $TiO_2(110)$ support. In the schematics of (b, d), the TiO_2 lattice is shown as gray rods separated by 2.94 Å in the [001] direction and 6.48 Å in [1$\bar{1}$0]. Pt atoms overlapping with the $TiO_2(110)$ surface unit cell are drawn in blue and highlighted by open black circles. The remaining Pt atoms are drawn in red. The data in (a) and (b) correspond to Pt NPs analogous to those in Figures 1a and 4a (TA, not rotated). Due to the 6-fold symmetry of the Pt(111) facet, the best overlap between both lattices was found at 0°, 60°, 120°, and 180°. For better visibility, only a cross sectional view of the complete plot is shown in (a). The overlap corresponds to a Pt(111) interfacial layer expanded by 6.4% in the [001] direction of $TiO_2(110)$ and contracted by 10.0% along [1$\bar{1}$0], as shown in (b). For the rotated TA NP in (c), the rotation angle was kept fixed to the STM-observed value (θ = 30°), and the strain parameters (ε_x and ε_y) were varied until a maximum overlap of NP and substrate lattice was obtained for ε_x = 1.7% and ε_y = 6.5% (c).

stresses (~6%) in the $TiO_2(110)$-[001] direction were obtained for the four NP shape categories resolved here via STM. Since the lattice of the free Pt surface is naturally under tensile stress,[50] the addition of interface-induced tensile stress is expected to increase the surface energy and, therefore, to decrease the area of the top facets parallel to the NP/support interface. This might explain why NPs of type A and C with top (111) facets are characterized by A_{100}/A_{111} ratios higher than the bulklike Wulff structures, while type B NPs with (100) top and interfacial facets show smaller relative A_{100}/A_{111} ratios. In Figure 5, the A_{100}/A_{111} ratios of TA NPs are centered around 0.3 ($\gamma_{100}/\gamma_{111}$ = 1.15) and 0.5 ($\gamma_{100}/\gamma_{111}$ = 1.05). On the basis of ab initio calculations, Iddir et al.[34] explained variations in this ratio for Pt NPs supported on $SrTiO_3$ due to a {100} hexagonal surface reconstruction. Such surface reconstruction is likely sensitive to environmental fluctuations (e.g., presence of adsorbates or encapsulation effects of the NPs by the underlying substrate), and reconstructed and nonreconstructed NP surfaces could coexist on one sample, resulting in a category of shapes (TA) with two different A_{100}/A_{111} ratios. The one with a higher fraction of {100} facets might correspond to the reconstructed (or support-encapsulated) surface with the minimum surface energy.[34]

dx.doi.org/10.1021/nl2027525 |*Nano Lett.* 2011, 11, 5290–5296

The Pt/TiO_2 system is known to display SMSI effects[51] and therefore, Pt NPs might be subjected to TiO_x[31,52,53] encapsulation or surface alloying effects[30] (e.g., Pt_3Ti) after annealing at high temperature. However, we do not believe that the shapes reported here for Pt NPs can be attributed to SMSI, since similar NP shapes were also observed for our micellar Au NPs on TiO_2(110) (Figure 3), even though the latter system does not show SMSI.

The energy barrier between different crystalline configurations is expected to increase with increasing NP size, and therefore, smaller NPs are expected to adopt their equilibrium shapes at lower temperature.[54] Within the size and temperature ranges of this study (2 nm < NPs < 6 nm, ~1000 °C), the energy barrier appears to be small enough to let the NPs stabilize in only a few geometrical configurations, but not small enough to allow them to adopt the shape with the interfacial facet that has the minimum interfacial energy.

Conclusions. We have shown that geometrically well-defined faceted and epitaxial Pt and Au NPs can be obtained on TiO_2-(110) via inverse micelle encapsulation methods followed by annealing in vacuum above 1000 °C. Despite the existence of significant anisotropic interfacial strain, our NPs were found to be symmetric and of single crystal nature. The micellar NPs adopt shapes that have not been previously observed for analogous but physical vapor deposited NPs. The epitaxial orientation of the interfacial facets observed and rare occurrence of rotated NPs were explained based on calculations of lattice mismatch. Moreover, the surface area and related surface energy ratios (A_{100}/A_{111} and $\gamma_{100}/\gamma_{111}$) in the micellar NPs were found to be different from conventional bulklike Wulff structures. Some of our Pt NPs displayed higher Miller index surfaces such as {110}, and tilted Au NPs were characterized by {221} interfacial facets.

Our study demonstrates that the shape of micellar NPs and their interfacial epitaxy can be controlled by tuning the NPs size. Such control over the size, shape, homogeneous dispersion on the support, and interfacial epitaxy represents a significant advance in our ability to engineer active elements at the nanoscale such as tunable nanoelectronic devices and nanocatalysts. Furthermore, the thermodynamically stable morphology of our NPs guarantees the stability of bottom-up-built nanodevices under extreme operation conditions, including elevated temperatures, and provides an excellent platform for theoretical calculations based on equilibrium NP shapes.

■ ASSOCIATED CONTENT

Supporting Information. Detailed description of the methods used to reconstruct the shapes of the NPs and to determine their epitaxial orientation and strain values obtained for different Pt and Au facets in contact with the rutile TiO_2(110) support surface. This material is available free of charge via the Internet at http://pubs.acs.org.

■ AUTHOR INFORMATION

Corresponding Author
*E-mail: roldan@ucf.edu.

■ ACKNOWLEDGMENT

Funding for this work was provided by the US National Science Foundation (NSF-DMR-1006232).

■ REFERENCES

(1) Henry, C. R. *Surf. Sci. Rep.* **1998**, *31* (7−8), 235–325.
(2) Campbell, C. T. *Surf. Sci. Rep.* **1997**, *27* (1−3), 1–111.
(3) Mostafa, S.; Behafarid, F.; Croy, J. R.; Ono, L. K.; Li, L.; Yang, J. C.; Frenkel, A. I.; Roldan Cuenya, B. *J. Am. Chem. Soc.* **2010**, *132* (44), 15714–15719.
(4) Roldan Cuenya, B. *Thin Solid Films* **2010**, *518* (12), 3127–3150.
(5) Rioux, R. M.; Song, H.; Grass, M.; Habas, S.; Niesz, K.; Hoefelmeyer, J. D.; Yang, P.; Somorjai, G. A. *Top. Catal.* **2006**, *39* (3−4), 167–174.
(6) Komanicky, V.; Iddir, H.; Chang, K. C.; Menzel, A.; Karapetrov, G.; Hennessy, D.; Zapol, P.; You, H. *J. Am. Chem. Soc.* **2009**, *131* (16), 5732–5733.
(7) Christopher, P.; Linic, S. *J. Am. Chem. Soc.* **2008**, *130* (34), 11264–11265.
(8) Naitabdi, A.; Ono, L. K.; Roldan Cuenya, B. *Appl. Phys. Lett.* **2006**, *89* (4), 043101.
(9) Zou, J. J.; Chen, C.; Liu, C. J.; Zhang, Y. P.; Han, Y.; Cui, L. *Mater. Lett.* **2005**, *59* (27), 3437–3440.
(10) Strasser, P.; Koh, S.; Anniyev, T.; Greeley, J.; More, K.; Yu, C. F.; Liu, Z. C.; Kaya, S.; Nordlund, D.; Ogasawara, H.; Toney, M. F.; Nilsson, A. *Nat. Chem.* **2010**, *2* (6), 454–460.
(11) Mei, Q. S.; Lu, K. *Prog. Mater. Sci.* **2007**, *52* (8), 1175–1262.
(12) Steinruck, H. P.; Pesty, F.; Zhang, L.; Madey, T. E. *Phys. Rev. B* **1995**, *51* (4), 2427–2439.
(13) Roldan Cuenya, B.; Croy, J. R.; Mostafa, S.; Behafarid, F.; L. Li, Z. Z.; Yang, J. C.; Wang, Q.; Frenkel, A. I. *J. Am. Chem. Soc.* **2010**, *132*, 8747.
(14) Cosandey, F.; Zhang, L.; Madey, T. E. *Surf. Sci.* **2001**, *474* (1−3), 1–13.
(15) Linsebigler, A.; Rusu, C.; Yates, J. T. *J. Am. Chem. Soc.* **1996**, *118* (22), 5284–5289.
(16) Tamura, K.; Owari, M.; Nihei, Y. *Bull. Chem. Soc. Jpn.* **1988**, *61* (5), 1539–1544.
(17) Besenbacher, F. *Rep. Prog. Phys.* **1996**, *59* (12), 1737–1802.
(18) Szoko, J.; Berko, A. *Vacuum* **2003**, *71* (1−2), 193–199.
(19) Berko, A.; Szoko, J.; Solymosi, F. *Surf. Sci.* **2003**, *532*, 390–395.
(20) Dulub, O.; Hebenstreit, W.; Diebold, U. *Phys. Rev. Lett.* **2000**, *84* (16), 3646–3649.
(21) Azatyan, S. G.; Iwami, M.; Lifshits, V. G. *Surf. Sci.* **2005**, *589* (1−3), 106–113.
(22) Spatz, J. P.; Mossmer, S.; Hartmann, C.; Moller, M.; Herzog, T.; Krieger, M.; Boyen, H. G.; Ziemann, P.; Kabius, B. *Langmuir* **2000**, *16* (2), 407–415.
(23) Haupt, M.; Miller, S.; Ladenburger, A.; Sauer, R.; Thonke, K.; Spatz, J. P.; Riethmuller, S.; Moller, M.; Banhart, F. *J. Appl. Phys.* **2002**, *91* (9), 6057–6059.
(24) Naitabdi, A.; Ono, L. K.; Behafarid, F.; Roldan Cuenya, B. *J. Phys. Chem. C* **2009**, *113* (4), 1433–1446.
(25) Roldan Cuenya, B.; Ono, L. K.; Croy, J. R.; Naitabdi, A.; Heinrich, H.; Zhao, J.; Alp, E. E.; Sturhahn, W.; Keune, W. *Appl. Phys. Lett.* **2009**, *95* (14), 143103.
(26) Ono, L. K.; Yuan, B.; Heinrich, H.; Roldan Cuenya, B. *J. Phys. Chem. C* **2010**, *114* (50), 22119–22133.
(27) Naitabdi, A.; Behafarid, F.; Roldan Cuenya, B. *Appl. Phys. Lett.* **2009**, *94* (8), 083102.
(28) Besenbacher, F.; Lauritsen, J. V.; Wendt, S. *Nano Today* **2007**, *2* (4), 30–39.
(29) Lai, X.; St Clair, T. P.; Valden, M.; Goodman, D. W. *Prog. Surf. Sci.* **1998**, *59* (1−4), 25–52.
(30) Tauster, S. J.; Fung, S. C.; Garten, R. L. *J. Am. Chem. Soc.* **1978**, *100* (1), 170–175.
(31) Pesty, F.; Steinruck, H. P.; Madey, T. E. *Surf. Sci.* **1995**, *339* (1−2), 83–95.
(32) Wulff, G. Z. *Kristallografiya* **1901**, *34*, 449.
(33) Enterkin, J. A.; Poeppelmeier, K. R.; Marks, L. D. *Nano Lett.* **2011**, *11* (3), 993–997.

(34) Iddir, H.; Komanicky, V.; Ogut, S.; You, H.; Zapol, P. *J. Phys. Chem. C* **2007**, *111* (40), 14782–14789.
(35) Yang, J. Y.; Hu, W. Y.; Chen, S. G.; Tang, J. F. *J. Phys. Chem. C* **2009**, *113* (52), 21501–21505.
(36) Yang, J. Y.; Hu, W. Y.; Chen, S. G. *Thin Solid Films* **2010**, *518* (14), 4041–4045.
(37) Henry, C. R. *Prog. Surf. Sci.* **2005**, *80* (3−4), 92–116.
(38) Hansen, P. L.; Wagner, J. B.; Helveg, S.; Rostrup-Nielsen, J. R.; Clausen, B. S.; Topsoe, H. *Science* **2002**, *295* (5562), 2053–2055.
(39) Goniakowski, J.; Jelea, A.; Mottet, C.; Barcaro, G.; Fortunelli, A.; Kuntova, Z.; Nita, F.; Levi, A. C.; Rossi, G.; Ferrando, R. *J. Chem. Phys.* **2009**, *130* (17), 174703.
(40) Iddir, H.; Ogut, S.; Browning, N. D.; Disko, M. M. *Phys. Rev. B* **2005**, *72* (8), 081407.
(41) Rodriguez, J. A.; Liu, G.; Jirsak, T.; Hrbek, J.; Chang, Z. P.; Dvorak, J.; Maiti, A. *J. Am. Chem. Soc.* **2002**, *124* (18), 5242–5250.
(42) Nguyen, V. L.; Nguyen, D. C.; Hayakawa, T.; Hirata, H.; Lakshminarayana, G.; Nogami, M. *Nanotechnology* **2010**, *21* (3), 035605.
(43) Li, Y. D.; Xu, R.; Wang, D. S.; Zhang, J. T. *Chem—Asian J.* **2006**, *1* (6), 888–893.
(44) Rashkeev, S. N.; Ginosar, D. M.; Petkovic, L. M.; Farrell, H. H. *Catal. Today* **2009**, *139* (4), 291–298.
(45) Yudanov, I. V.; Genest, A.; Rösch, N. *J. Cluster Sci.* 2011.
(46) Ikuhara, Y.; Pirouz, P. *Mater. Sci. Forum* **1996**, *207−209*, 121–124.
(47) Iddir, H.; Disko, M. M.; Ogut, S.; Browning, N. D. *Micron* **2005**, *36* (3), 233–241.
(48) Muller, P.; Kern, R. *Appl. Surf. Sci.* **2000**, *164*, 68–71.
(49) Muller, P.; Kern, R. *Surf. Sci.* **2000**, *457* (1−2), 229–253.
(50) Wan, J.; Fan, Y. L.; Gong, D. W.; Shen, S. G.; Fan, X. Q. *Modell. Simul. Mater. Sci. Eng.* **1999**, *7* (2), 189–206.
(51) Tauster, S. J. *Acc. Chem. Res.* **1987**, *20* (11), 389–394.
(52) Datye, A. K.; Kalakkad, D. S.; Yao, M. H.; Smith, D. J. *J. Catal.* **1995**, *155* (1), 148–153.
(53) Bonanni, S. B., S.; Ait-Mansour, K.; Brune, H.; Harbich, W. *ACS Catal.* **2011**, *1* (4), 385–389.
(54) Marks, L. D. *Rep. Prog. Phys.* **1994**, *57* (6), 603–649.